RSC Advances

PAPER

View Article Online
View Journal | View Issue

Cite this: *RSC Adv.*, 2021, **11**, 16161

High mass loading flower-like MnO_2 on $NiCo_2O_4$ deposited graphene/nickel foam as high-performance electrodes for asymmetric supercapacitors†

Jing Jin,[ab] Jie Ding,[ab] Xing Wang,[c] Congcong Hong,[c] Huaping Wu,[ab] Min Sun,[ab] Xiehong Cao,[d] Congda Lu*[ab] and Aiping Liu*[c]

Received 31st December 2020
Accepted 20th April 2021

DOI: 10.1039/d0ra10948g

rsc.li/rsc-advances

The implementation of high mass loading MnO_2 on electrochemical electrodes of supercapacitors is currently challenging due to the poor electrical conductivity and elongated electron/ion transport distance. In this paper, a $NiCo_2O_4/MnO_2$ heterostructure was built on the surface of three-dimensional graphene/nickel foam (GNF) by a hydrothermal method. The petal structured $NiCo_2O_4$ loaded on graphene played a wonderful role as a supporting framework, which provided more space for the growth of high mass loading MnO_2 microflowers, thereby increasing the utilization rate of the active material MnO_2. The GNF@$NiCo_2O_4/MnO_2$ composite was used as a positive electrode and achieved a high areal capacitance of 1630.5 mF cm^{-2} at 2 mA cm^{-2} in the neutral Na_2SO_4 solution. The asymmetric supercapacitor assembled with the GNF@$NiCo_2O_4/MnO_2$ positive electrode and activated carbon negative electrode possessed a wide voltage window (2.1 V) and splendid energy density (45.9 Wh kg^{-1}), which was attributed to the satisfactory electroactive area, low resistance, quick mass diffusion and ion transport caused by high mass loading MnO_2.

Introduction

The research on portable supercapacitors has been given great attention owing to the high power density, fast charging and discharging, excellent cycling performance, indefinite lifespan, nonvulnerability to temperature change, nontoxicity in nature, and their being more reliable than batteries. According to the different charge-storage mechanisms, supercapacitors are divided into electric double-layer capacitors (EDLCs) and pseudocapacitors.[1–3] Compared with the carbon-based active materials for EDLCs, the pseudocapacitive electrode materials can provide higher specific capacitance and energy density which is related to specific capacitance and voltage window. Therefore, there are usually two strategies for increasing energy density, namely increasing specific capacitance and expanding the voltage window. Rational design of the nanostructure of the composites to increase the content and utilization of high-capacitance active materials per unit area of the electrode material is a feasible method.[4,5] Many composites of different pseudocapacitive materials and carbon materials with high specific capacitances have been researched, such as MnO_2/graphene/NF (NF, nickel foam),[6] RuO_2/graphene,[7] RuO_2/graphene/CNT (CNT, carbon nanotubes),[8] and V_2O_5-CNTs/GF (GF, graphene form)[9] with different morphologies.[10,11] Numerous studies have shown that combining MnO_2 with a highly conductive material to form a composite material can significantly enhance its electrical conductivity and electrochemical performance.[12–14] For example, Garakani *et al.* used GF substrates to grow $NiCo_2O_4/MnO_2$ arrays as a freestanding supercapacitor electrode with great enhancement in both gravimetric and areal capacitances.[15] Lu *et al.* obtained supercapacitors with good cycling performance using WO_{3-x}@Au@MnO_2 core–shell structure nanocomposites as electrodes.[16] Wang's group prepared composites of hierarchical $NiCo_2O_4/MnO_2$ nanosheets on carbo cloth which used as positive electrodes and achieved excellent electrochemical performance.[17] However, the specific capacitance mostly reported so far could be obtained just by loading a low mass MnO_2 (<1 mg cm^{-2}). Therefore, it's still urgent to load higher mass MnO_2 to acquire higher specific capacitance, higher energy density and wide

[a]College of Mechanical Engineering, Zhejiang University of Technology, Hangzhou 310023, China. E-mail: lcd@zjut.edu.cn

[b]Key Laboratory of Special Purpose Equipment and Advanced Processing Technology, Ministry of Education and Zhejiang Province, Zhejiang University of Technology, Hangzhou 310023, China

[c]Center for Optoelectronics Materials and Devices, Key Laboratory of Optical Field Manipulation of Zhejiang Province, Zhejiang Sci-Tech University, Hangzhou 310018, China. E-mail: liuaiping1979@gmail.com

[d]College of Materials Science and Engineering, Zhejiang University of Technology, Hangzhou 310018, China

† Electronic supplementary information (ESI) available. See DOI: 10.1039/d0ra10948g

voltage window in practical application.[18–22] In this paper, we designed heterogeneous $NiCo_2O_4/MnO_2$ materials on a graphene modified NF (GNF) substrate. The conductive petal-like $NiCo_2O_4$ arrays constructed on NF provided additional space to allow higher mass loading of MnO_2 micro-flowers. With GNF@$NiCo_2O_4/MnO_2$ composite material as the positive electrode and GNF@AC (AC, activated carbon) as the negative electrode, an asymmetric supercapacitor (ASC) was fabricated in a neutral Na_2SO_4 aqueous electrolyte. The electrode with high mass loading provides outstanding specific capacitance of 1630.5 mF cm^{-2} at 2 mA cm^{-2}. The assembled ASC shows excellent cycling performance, with its voltage window of 2.1 V, and the energy density of 505.2 μWh cm^{-2} (45.9 Wh kg^{-1}, 5.1 mWh cm^{-3}), demonstrating its application potential in the field of energy storage.

Experimental section

Growth of graphene on Ni foam (GNF)

Fig. 1 shows the synthesis process of GNF@$NiCo_2O_4/MnO_2$ electrode. First, graphene layer was deposited on the surface of NF by radio-frequency plasma enhanced chemical vapor deposition system (RF-PECVD).[23–27] Three pieces of NF with the area of 1 × 2 cm^2 and the thickness of 0.5 mm were ultrasonically cleaned in acetone, 1 M HCL and ethanol, and blown dried with moisture-free air. The quartz boat with NF substrates was then placed in the heating zone of RF-PECVD. The chamber was evacuated to a pressure less than 300 mTorr and then hydrogen gas was introduced at a rate of 6 sccm. Plasma was generated for 10 min with the RF power of 300 W to further remove contaminants on the substrates. When heating the chamber to 750 °C, graphene layer was grown by introducing CH_4, Ar and H_2 at flow rates of 10 sccm for 30 min under a plasma power of 250 W and a total pressure of ~400 mTorr. After the temperature was lowered to room temperature at a frequency of 10 °C min^{-1}, the GNF was obtained.

Preparation of GNF@$NiCo_2O_4$ and GNF@$NiCo_2O_4/MnO_2$

Petal shaped $NiCo_2O_4$ nanoarrays were deposited on GNF by using hydrothermal method. Typically, $Co(NO_3)_2 \cdot 6H_2O$ (1 mmol), $Ni(NO_3)_2 \cdot 6H_2O$ (2 mmol) and urea (12 mmol) were added into 100 mL deionized (D.I.) water and stirred for 30 minutes to obtain a homogenous mixed solution. GNF was treated with plasma for 100 s to make it hydrophilic and ready for use. Subsequently, a piece of treated GNF and 10 mL of the mixed solution were put into a Teflon-lined stainless-steel autoclave. The autoclave was heated to 160 °C in the oven and kept it for 10 h, 15 h, 20 h and 25 h, respectively, followed by naturally cooled to room temperature. The obtained precursors were washed repeatedly with D.I. water and ethanol, thereafter desiccated in the oven at 60 °C for 12 h. Lastly, the precursors were annealed in atmosphere at 300 °C for two hours to obtain petal-like GNF@$NiCo_2O_4$. By weighing the GNF before and after $NiCo_2O_4$ deposition, the mass loading of $NiCo_2O_4$ obtained under different reaction time was obtained. Furthermore, GNF@$NiCo_2O_4/MnO_2$ was prepared by the second hydrothermal treatment. The $KMnO_4$ (0.45 g) was added into D.I. water (10 mL), and was stirred for 30 minutes to obtain purple solution. The solution was placed in an autoclave simultaneously with as-synthesized GNF@$NiCo_2O_4$, heated to 160 °C and maintained for 10 hours, then freely cooled to ambient temperature. After that, the resulting compound was washed repeatedly to remove the residue and desiccated in oven at 60 °C for 12 hours, then GNF@$NiCo_2O_4/MnO_2$ was obtained. As a control, we also synthesized GNF@MnO_2 (without $NiCo_2O_4$) and NF@$NiCo_2O_4/MnO_2$ (without graphene) under the same conditions.

Fabrication of GNF@$NiCo_2O_4/MnO_2$//AC asymmetric pseudocapacitor

The formula for balancing the charge between the positive and negative electrodes is as follows:[28,29]

$$q = C \times \Delta V \times m \quad (1)$$

$$q^+ = q^- \quad (2)$$

where C and ΔV are the specific capacitance and charge/discharge potential range of each electrode, respectively. AC, acetylene black and polyvinylidene fluoride (PVDF) binder were mixed evenly into a slurry according to the weight ratio of 8 : 1 : 1, and then pressed on NF to construct the negative electrode. Next, it was dried in an oven at 60 °C for 10 hours. The positive electrode, negative electrode and separator were cut into 1 × 1 cm^2 size and 1 M Na_2SO_4 was used as the electrolyte to assemble the CR2018 coin cell.

Materials characterization

To determine the morphology and microstructural characteristic of the products, Hitachi S-4800 field emission scanning electron microscope (FE-SEM) was employed. The crystalline structures of samples were examined by a Bruker D8 Discover X-ray powder diffractometer (XRD, Cu K_α, λ = 0.15418 nm). The valence state of the composite was measured by X-ray

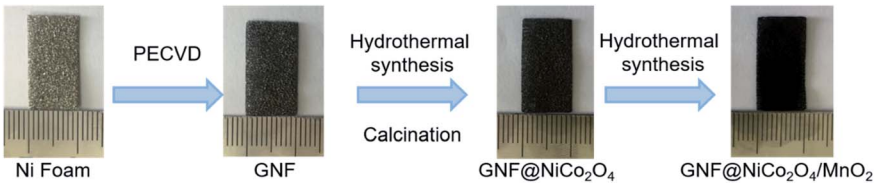

Fig. 1 Schematic of the synthesis process of GNF@$NiCo_2O_4/MnO_2$.

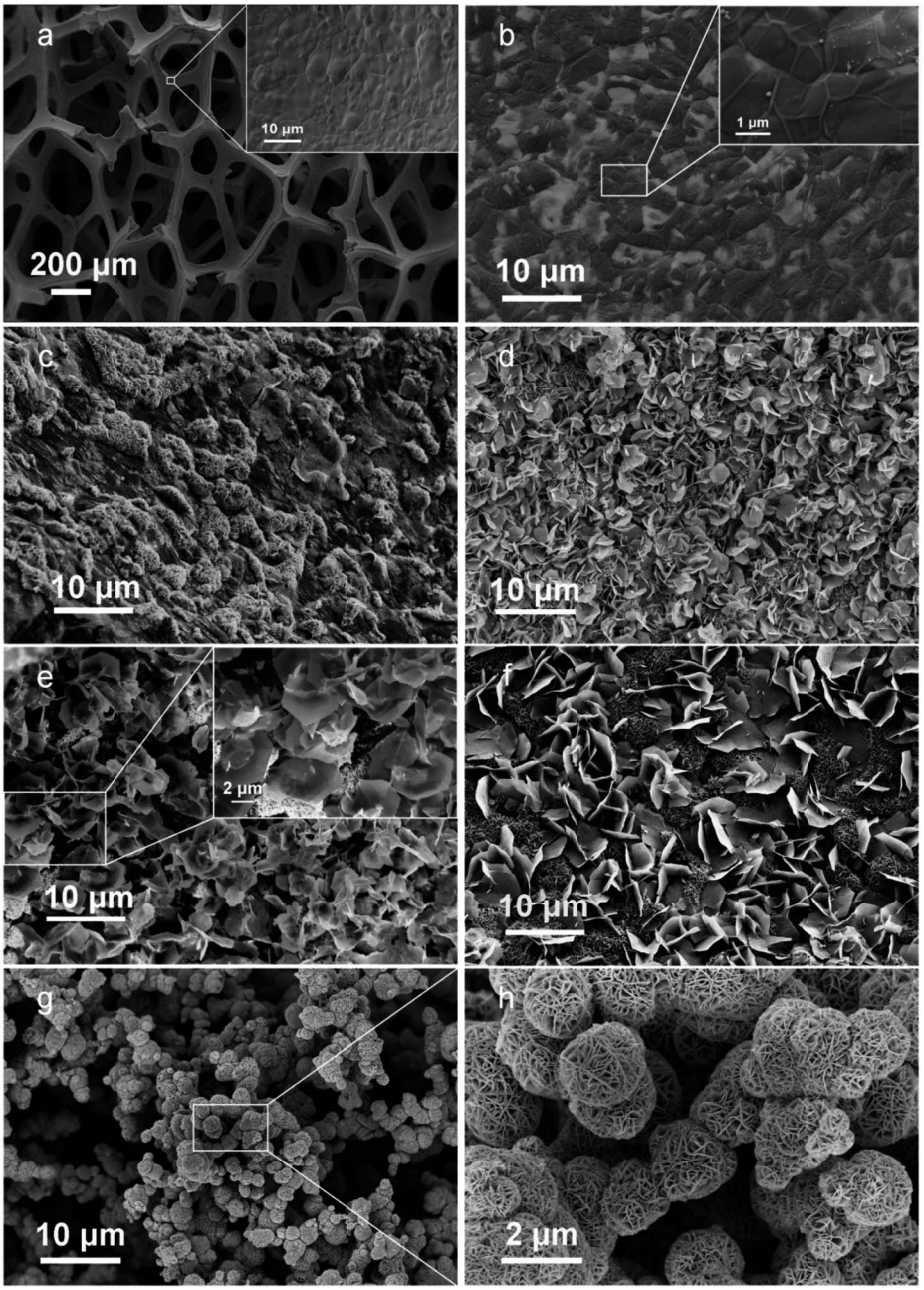

Fig. 2 SEM images of (a) bare Ni foam, (b) GNF, (c) GNF@$NiCo_2O_4$-10 h, (d) GNF@$NiCo_2O_4$-15 h, (e) GNF@$NiCo_2O_4$-20 h, (f) GNF@$NiCo_2O_4$-25 h, (g and h) GNF@$NiCo_2O_4$/MnO_2.

photoelectron spectrometer (XPS, Thermo Scientific ESCALAB 250Xi). Brunauer–Emmett–Teller (BET) surface area and Barrett–Joyner–Halenda (BJH) pore-size distribution analysis were carried out by a surface area analyzer (Autosorb-iQ). Lab RAM HR-Evolution (Horiba, 532 nm laser excitation) Raman spectrometer was utilized to investigate the Raman spectra of graphene. The mass loading was obtained by measuring the mass change of the sample before and after the reaction with a microbalance. Specially, the mass loading of graphene was 0.1 mg cm^{-2} in the obtained GNF; it was determined to be about 1.4 mg cm^{-2} of $NiCo_2O_4$ for the obtained GNF@$NiCo_2O_4$ (hydrothermal reaction time was 20 hours); the mass loadings of MnO_2 for GNF@MnO_2 and GNF@$NiCo_2O_4$/MnO_2 were 3.0 mg cm^{-2} and 3.5 mg cm^{-2}, respectively. Hence, the total mass loading of active materials for GNF@$NiCo_2O_4$/MnO_2 achieved 5.0 mg cm^{-2}. The mass loading of negative electrode was 6.0 mg cm^{-2}.

Electrochemical measurements

The electrochemical test was performed using 760E electrochemical workstation (CH instrument, China). The electrochemical property of single electrode was examined under there-electrode configuration in 1 M Na_2SO_4 solution. A Pt foil was applied as counter electrode and saturated calomel

electrode (SCE) electrode was employed as reference electrode. The electrochemical impedance spectroscopy (EIS) was analyzed at the open circuit potential in frequency range from 0.01 Hz to 100 kHz. Cyclic voltammetry (CV) and galvanostatic charge–discharge (GCD) measurements were performed in the operating potential range of 0–0.8 V. The specific capacitance (C_s, C_m) is calculated by the following formulas (3) and (4) using GCD data.[30–32]

$$C_s = \frac{I \times \Delta t}{s \times \Delta V} \quad (3)$$

$$C_m = \frac{I \times \Delta t}{m \times \Delta V} \quad (4)$$

where I (mA), Δt (s), s (cm^2), m (g), and ΔV (V) represent the discharge current, discharge time, area, loading mass, and voltage window, respectively. The cycling capacity retention rate was the ratio between the final capacity and the initial one. The energy density E of the ASC was calculated by eqn (5), and (6) was used to calculate the power density:[33–35]

$$E = \frac{1}{2} C V^2 \quad (5)$$

$$P = \frac{E}{\Delta t} \quad (6)$$

where C represented the specific capacitance obtained from above equations, and V and t were the voltage window and discharge time, respectively.

Results and discussion

Morphologies and structures of GNF@$NiCo_2O_4$/MnO_2

High-quality graphene was obtained by adjusting the gas flow rate, the reaction gas ratio, the reaction time, and the radio frequency power during the reaction *via* RF-PECVD system. Fig. 2a and b show the morphology of the bare NF surface before and after the deposition of graphene. Clear graphene wrinkles are uniformly covered on the 3D NF network. From the SEM images of GNF@$NiCo_2O_4$ in Fig. 2c–f, it is found that the GNF is covered by $NiCo_2O_4$ sheet arrays through hydrothermal treatment. As the reaction time increases, the surface morphology of GNF@$NiCo_2O_4$ changes significantly. When the reaction is carried out for 10 hours, some scattered flaky networks are overlaid on GNF. After 15 hours, large sheets begin to grow between the flaky networks, and form new network arrays. When the time reaches 20 hours, the large petal-like microsheets form a 3D layered framework, which is beneficial for further deposition of new materials. After 25 hours of reaction, the larger sheets are scattered on the top of the network formed by the smaller sheets and do not form an orderly network. When MnO_2 is deposited on the surface of GNF@$NiCo_2O_4$ (reaction time of 20 hours), the flower-like MnO_2 microspheres are evenly dispersed on the $NiCo_2O_4$ nanosheet arrays, as shown in Fig. 2g and h. The microspheres are also formed by many sheets, which provides a 3D structure and is beneficial for electron transmission and ion diffusion. The microstructures were also characterized by the Raman spectrum and XRD pattern. From

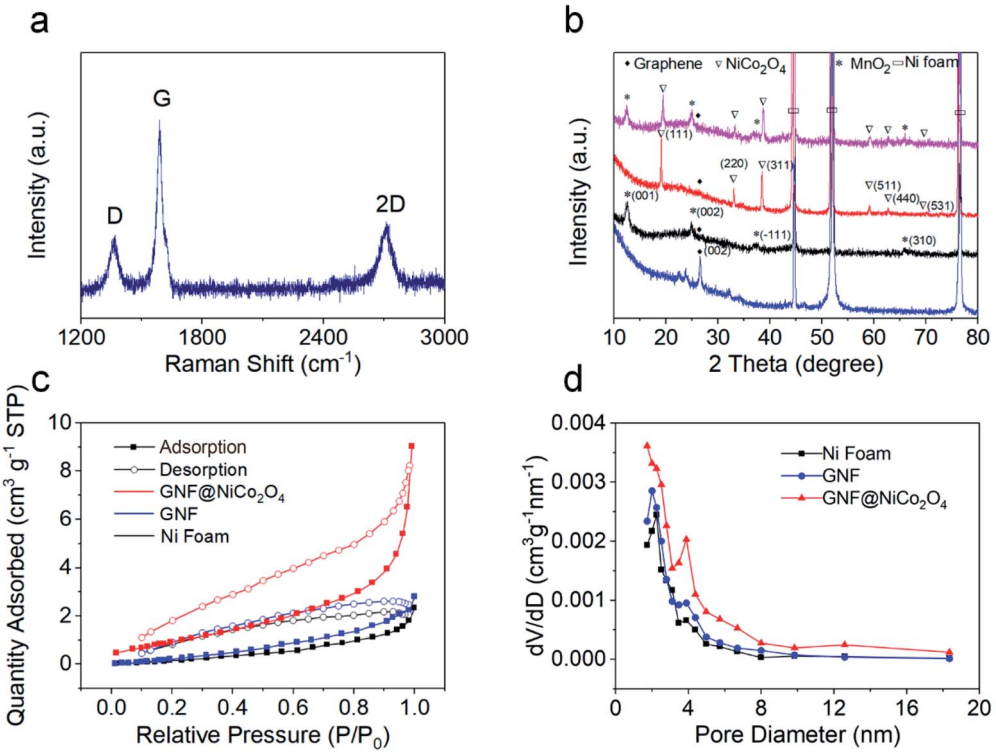

Fig. 3 (a) Raman spectra of GNF, (b) XRD patterns of GNF (blue line), GNF@MnO_2 (black line), GNF@$NiCo_2O_4$ (red line), and GNF@$NiCo_2O_4$/MnO_2 (pink line). (c and d) The nitrogen adsorption/desorption isotherms and the corresponding BJH pore size distribution of Ni foam (black line), GNF (red line), and GNF@$NiCo_2O_4$ (blue line).

the Raman spectrum of GNF in Fig. 3a, it shows the characteristic D, G, and 2D peaks located at 1353 cm^{-1}, 1580 cm^{-1}, and 2702 cm^{-1}, respectively. The position of Raman peak and the intensity ratio of graphene will be affected by defects and the number of graphene layers.[36] The D band is disordered sp^2 C in graphene.[37] The intensity ratio of the D band to the G band ($I_D/I_G = 0.27$) indicates the graphene with few defects.[38] The peak at 1580 cm^{-1} (G band) stands for sp^2 C in graphene, and the I_G/I_{2D} ratio of 2.05 represents its multi-layer structure.[39,40] The XRD pattern of GNF (Fig. 3b blue line) presents a sharp peak at $2\theta \approx 26.4°$, which corresponds to (002) reflection of graphene (JCPDS 75-1621).[41] For GNF@$NiCo_2O_4$-20 h samples, in addition to the three typical peaks of Ni, another six well-defined diffraction peaks are shown at 2θ equalling to ~19.0° (111), 32.9° (220), 38.4° (311), 59.1° (511), 62.7° (440) and 69.4° (531), which represent the spinel crystalline structure of $NiCo_2O_4$ (JCPDS file no. 20-0781).[42] The XRD pattern of GNF@MnO_2 (black line in Fig. 3b) shows that the diffraction peaks near to 12.3°, 24.8°, 37.3°, and 65.9° can well match (001), (002), (−111), and (310) planes of monoclinic birnessite-type MnO_2 (JCPDS 42-1317).[43,44] The XRD pattern of the GNF@$NiCo_2O_4$/MnO_2 (the pink line in Fig. 3b) shows a small peak at $2\theta \approx 26.4°$ corresponding to the graphene and other characteristic peaks related to crystallographic planes of $NiCo_2O_4$ (JCPDS 020-0781) and MnO_2 (JCPDS 42-1317). The surface areas and pore size of the samples were measured by nitrogen adsorption/desorption tests. The specific surface area of GNF@$NiCo_2O_4$ is 13.02 $m^2\ g^{-1}$ calculated by Brunauer–Emmett–Teller (BET) method, which is two times higher than that of GNF (Fig. 3c). It indicates that the presence of $NiCo_2O_4$ effectively increases the specific surface area of the composite. Barrett–Joyner–Halenda (BJH) pore size distribution shows the

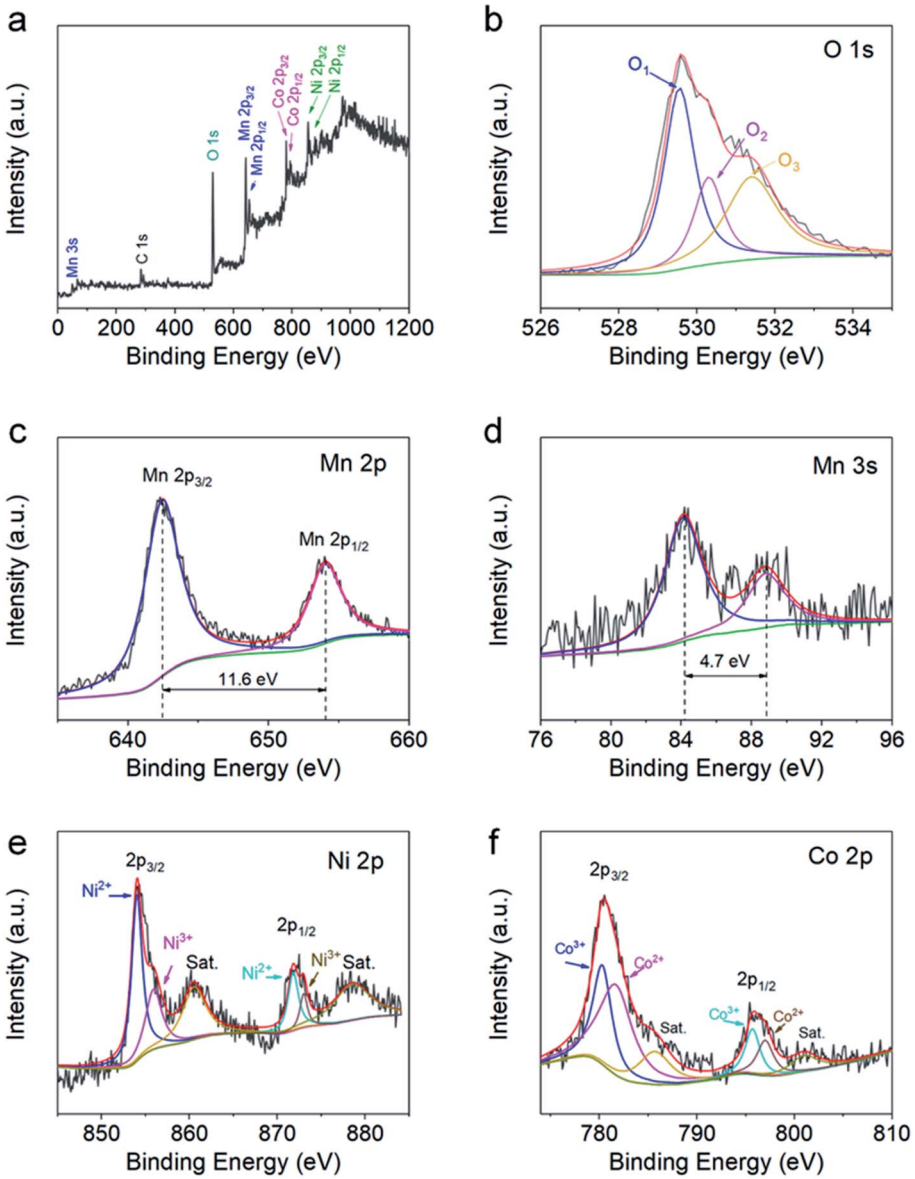

Fig. 4 XPS spectra of GNF@$NiCo_2O_4$/MnO_2. (a) Survey scan, (b) O 1s, (c) Mn 2p, (d) Mn 3s, (e) Ni 2p, and (f) Co 2p core level spectra.

microporous and mesoporous of GNF@$NiCo_2O_4$ are distributed in 1.7–8.0 nm range (Fig. 3d).[45–47] The 3D structure of GNF@$NiCo_2O_4$ increases the distribution space of MnO_2, thereby increasing the surface area of MnO_2 in contact with the electrolyte, providing more electron transport channels and shortening the electron/ion transport distance.

The chemical composition of GNF@$NiCo_2O_4$/MnO_2 was also investigated by XPS measurement. Fig. 4a shows the survey spectrum, indicating the presence of C, Mn, O, Ni, and Co elements. Fig. 4b shows that the O 1s core level spectrum of the prepared GNF@$NiCo_2O_4$/MnO_2 and can be divided into three characteristic peaks, namely O_1, O_2 and O_3 located at 529.5 eV, 530.3 eV and 531.4 eV, respectively. The fitted peak O_1 can be attributed to the lattice O^{2-}, which corresponds to a typical metal–oxygen bond.[48] The peak of O_2 is associated with the surface oxygen in OH^-.[49] The O_3 peak is related to oxygen ions with low coordination on the surface of metal oxides, and formally these oxide ions are O^- species with lower electron density than the classical O^{2-} ions.[50] Fig. 4c is the scanning spectrum of Mn 2p.

Two distinct characteristic peaks located at 642.4 eV and 654.0 eV correspond to Mn $2p_{3/2}$ and Mn $2p_{1/2}$, respectively. The distance between the two peaks is about 11.6 eV, which confirms the formation of MnO_2.[51] In the Mn 3s spectrum (Fig. 4d), the peaks are observed near 84.1 eV and 88.8 eV, the energy separation of 4.7 eV further indicates that the Mn element in the sample mainly exists in the form of +4 valence.[52] Fig. 4e shows the scanning spectrum of the Ni 2p energy level, showing two distinct main peaks corresponding to Ni $2p_{3/2}$ and Ni $2p_{1/2}$. The two fitted peaks placed at 854.0 eV and 871.8 V correspond to Ni^{2+}, and the two peaks at 855.9 eV and 873 eV correspond to Ni^{3+}. The satellite peaks located at 860.5 eV and 878.5 eV are indicators of the two shake-type peaks of Ni.[53,54] The Co 2p spectrum (Fig. 4f) similarly shows two spin–orbit double peaks and two satellite peaks. The two main peaks are attributed to Co $2p_{3/2}$ and Co $2p_{1/2}$. Among them, the two fitted peaks at 781.7 V and 797 eV are attributed to Co^{2+}, while the other two at 780.3 eV and 797.0 eV belong to Co.[3] The two satellite peaks are located at 785.7 eV and 801.0 eV.[55]

Supercapacitive performance of electrodes

To investigate the electrochemical properties of the materials, the composites were immersed in a three-electrode configuration by adopting it as the working electrode. Fig. S1† provides the CV curves of pure NF at different scan rates. The areas of the CV curves are very small, which indicates that pure NF has a low capacity. The effect of hydrothermal reaction time on the electrochemical performance of GNF@$NiCo_2O_4$ was explored at the same scanning frequency. As shown in Fig. 5a, the current response of GNF@$NiCo_2O_4$ with 20 hours hydrothermal reaction is the largest, showing that the sample may possess the highest specific capacitance. This is verified by the GCD curves

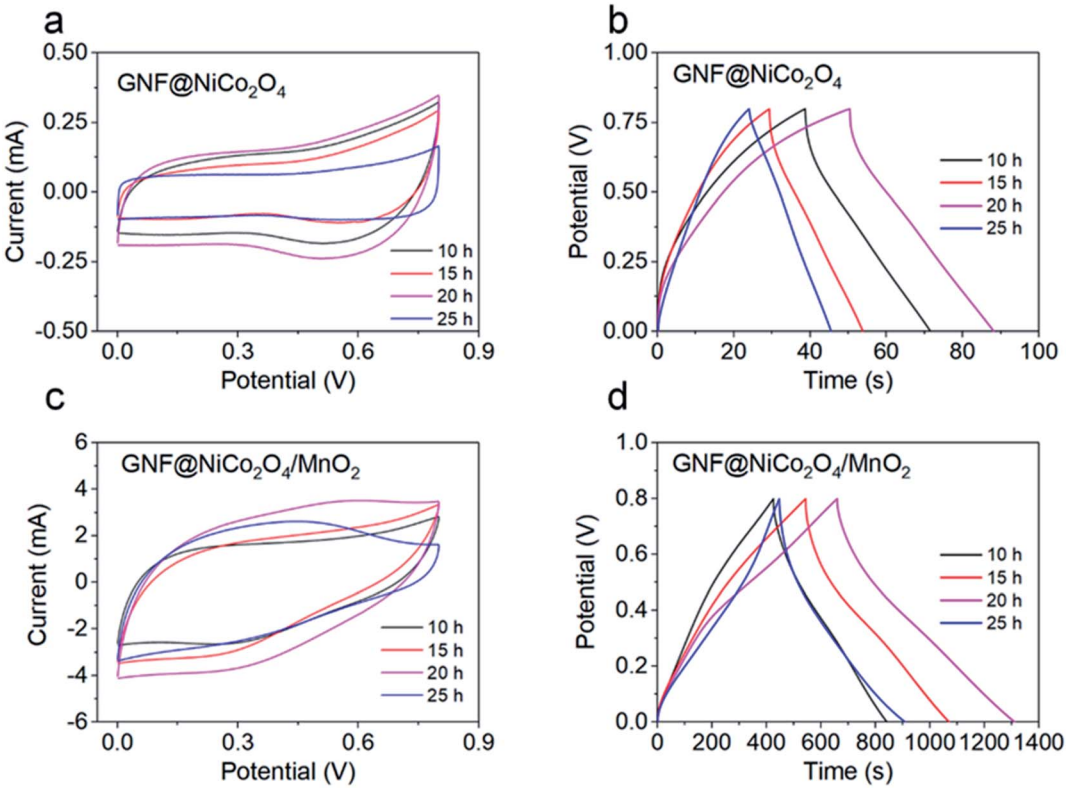

Fig. 5 (a) The CV curves of GNF@$NiCo_2O_4$ electrodes with different reaction time at 5 mV s^{-1}, (b) the GCD curves of GNF@$NiCo_2O_4$ electrodes with different reaction time at 2 mA cm^{-2}, (c) the CV curves of different GNF@$NiCo_2O_4$/MnO_2 electrodes at 10 mV s^{-1}, (d) the GCD curves of different GNF@$NiCo_2O_4$/MnO_2 electrodes at 2 mA cm^{-2}.

which shows the relationship between the discharge time of different GNF@$NiCo_2O_4$ samples and hydrothermal reaction time (Fig. 5b). The longest discharge time of the GNF@$NiCo_2O_4$-20 h proves its highest area specific capacitance. But the CV curve of GNF@$NiCo_2O_4$ does not show a clear redox peak, and the GCD curve has no sloping plateau, indicating that its redox-active is suppressed in salt solutions, and its short charge and discharge time also prove this result.

When MnO_2 was deposited on the GNF@$NiCo_2O_4$ with different reaction time for 10 hours to obtain different GNF@$NiCo_2O_4$/MnO_2 composites, the CV curve (Fig. 5c) and GCD curve (Fig. 5d) of the sample with GNF@$NiCo_2O_4$-20 h are more symmetrical rectangular and triangular than other samples, indicating the pseudocapacitive properties of the electrode are primarily attributed to the two electron-transferred charge storage mechanism of MnO_2 in the mild Na_2SO_4 aqueous electrolyte. This involves surface adsorption/desorption and the reversible redox transition, the exchange of protons and/or cations with the electrolyte and different oxidation states, and can be expressed as follows

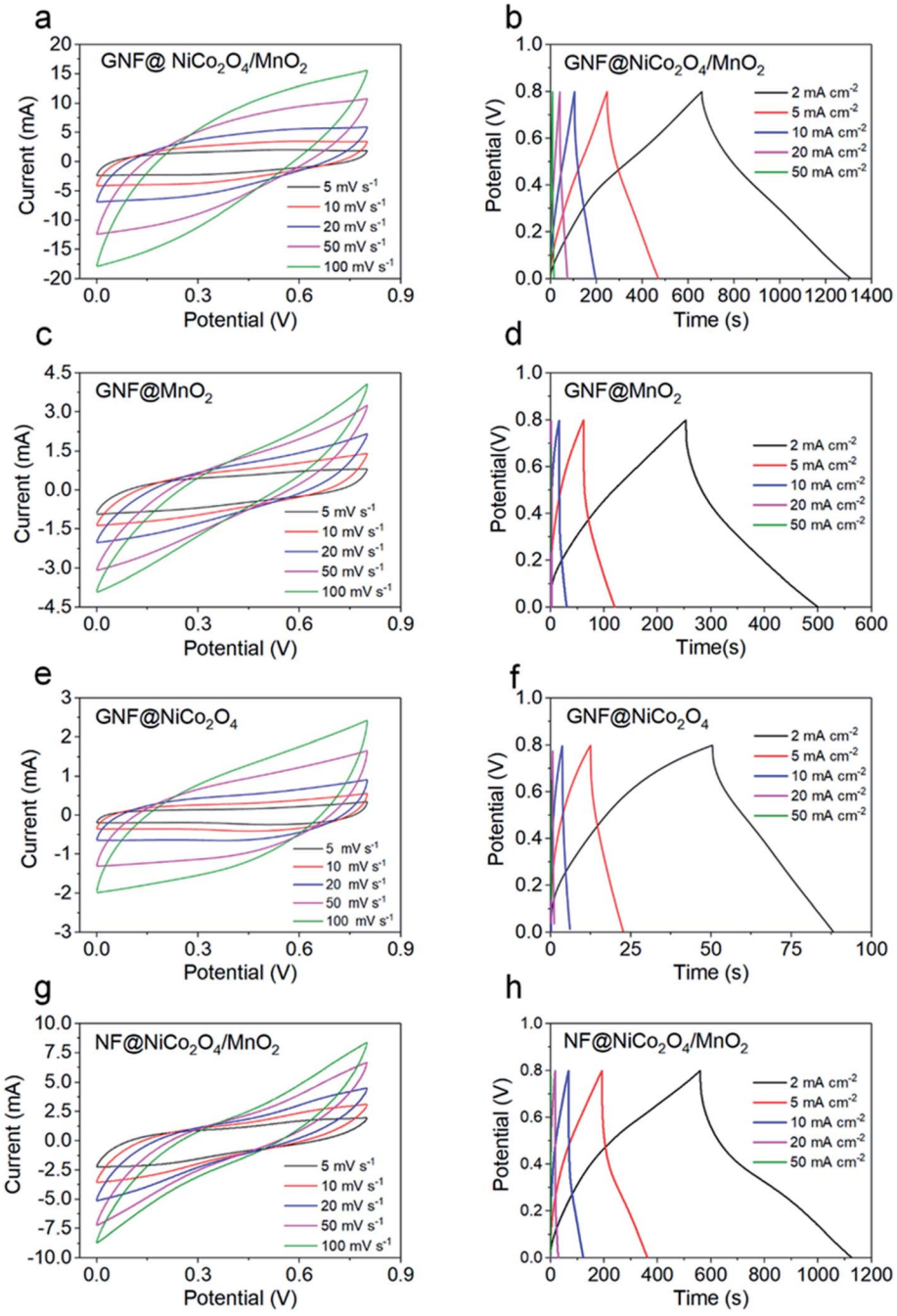

Fig. 6 (a, c, e and g) CV curves of GNF@$NiCo_2O_4$/MnO_2, GNF@MnO_2, GNF@$NiCo_2O_4$ and NF@$NiCo_2O_4$/MnO_2 samples at different scan rates, (b, d, f and h) GCD curves of GNF@$NiCo_2O_4$/MnO_2, GNF@MnO_2, GNF@$NiCo_2O_4$ and NF@$NiCo_2O_4$/MnO_2 samples at different current densities.

$$(MnO_2)_{surface} + Na^+ + e^- \leftrightarrow (MnO^-Na^+)_{surface},$$
$$MnO_2 + Na^+ + e^- \leftrightarrow MnOONa \quad (7)$$

The composite material with GNF@$NiCo_2O_4$-20 h has the largest CV curve area and the longest discharge time among all composites, revealing that it has the highest specific capacitance. Therefore, it is used in the following study.

The electrochemical properties of the GNF@$NiCo_2O_4$/MnO_2, GNF@$NiCo_2O_4$, GNF@MnO_2 and NF@$NiCo_2O_4$/MnO_2 were studied in detail. Fig. 6 shows the CV and GCD curves of these electrodes. A largest integrated area in CV and longest discharging time in GCD curves of the GNF@$NiCo_2O_4$/MnO_2 electrode demonstrate its best electrochemical performance in comparison with GNF@$NiCo_2O_4$, GNF@MnO_2 and NF@$NiCo_2O_4$/MnO_2. Rectangular-like CV shapes of GNF@$NiCo_2O_4$/MnO_2 reveal good capacitive reversibility, and the triangular symmetry of GCD curves hints its excellent pseudocapacitive properties. Meanwhile, its nearly symmetric GCD profiles and the lower IR drop than other samples suggest favourable conductivity. Fig. 7a illustrates the specific capacitances of these samples obtained by the GCD data. It can be observed that the GNF@$NiCo_2O_4$/MnO_2 delivers higher specific capacitance of 1630.5, 1402.5, 1150.0, 832.5, and 387.5 mF cm^{-2}, compared to only 94.5, 63.75, 30.0, 12.5 and 10.0 mF cm^{-2} for the GNF@$NiCo_2O_4$, 619.3, 366.3, 172.5, 25.0 and 11.1 mF cm^{-2} for the GNF@MnO_2, and 1422.3, 1067.5, 690.0, 292.5, and 18.8 mF cm^{-2} for the NF@$NiCo_2O_4$/MnO_2 at current densities of 2, 5, 10, 20 and 50 mA cm^{-2}, respectively. Note that the areal capacitance of GNF@$NiCo_2O_4$ is almost negligible. The areal specific capacitance of GNF@$NiCo_2O_4$/MnO_2 is 17.3 and 2.6 times higher than those of GNF@$NiCo_2O_4$ and GNF@MnO_2 at 2 mA cm^{-2}, respectively. The mass loading of MnO_2 has increased from 3 mg cm^{-2} of GNF@MnO_2 to 3.5 mg cm^{-2} of GNF@$NiCo_2O_4$/MnO_2. The increase in mass loading is very small, but the areal capacitance of the composite has increased by 2.6 times than GNF@MnO_2. It can be seen that the increase in capacitance is not caused by the increase in the mass loading of MnO_2, but the structure of GNF@$NiCo_2O_4$/MnO_2 effectively improves the utilization of the active MnO_2. The petal structured $NiCo_2O_4$ provides large surface area for the high mass loading of MnO_2 and more electron transmission channels to MnO_2, and reduces the accumulation of MnO_2. As a result, the capacitance utilization of MnO_2 is improved and the areal capacitance of the composite material increases.[56] In addition, it is observed that when the current density increases from 2 mA cm^{-2} to 20 mA cm^{-2}, the original surface capacitance of the GNF@$NiCo_2O_4$/MnO_2 loses 48.9%, demonstrating its outstanding rate capability. The specific capacitance of NF@$NiCo_2O_4$/MnO_2 is only 208.3 mF cm^{-2} lower than that of GNF@$NiCo_2O_4$/MnO_2 at 2 mA cm^{-2}. However, its areal capacitance drops by nearly 80% from 2 to 20 mA cm^{-2}, illustrating its poor rate performance. This demonstrates that the graphene effectively improves the rate performance of the electrodes. The EIS test was conducted to estimate charge transfer kinetics of the hybrid materials and the obtained Nyquist plots are given in Fig. 7b. In general, the equivalent series resistance (ESR, R_s) of an electrode can be determined by observing the EIS spectrum in the high frequency region. It includes the inherent resistance of the electrode material (both current collector and active material), the contact resistance of the electrode/electrolyte interface and the bulk resistance of the electrolyte, and its value depends on the intercept of the spectrum on the transverse axis. That is, the R_s of the electrode can be seen at the intersection of the transverse axis.[57] The semicircle in the Nyquist plot can be used to determine the charge transfer resistance R_{ct}, the larger the diameter of the semicircle, the larger R_{ct} of the electrode.[58] The GNF@$NiCo_2O_4$/MnO_2 electrode reveals a smaller equivalent series resistance R_s (5.3 Ω) and charge transfer resistance R_{ct} (10.4 Ω) compared to that of GNF@MnO_2 (R_s 5.7 Ω, R_{ct} 55.7), suggesting its better electrical conductivity and rapid charge mobility. Low frequency range is related to the Warburg impedance which reflects the ion diffusion/transport in the electrolyte.[59] The slope of GNF@$NiCo_2O_4$/MnO_2 is higher than that of GNF@MnO_2, indicating its lower diffusion resistance. These results further convincingly prove that the existence of petal structured $NiCo_2O_4$ as skeleton for the depositing of MnO_2 can effectively decrease the internal resistance and facilitate the electron transfer, which is beneficial to promote the areal capacitance of the hybrid GNF@$NiCo_2O_4$/MnO_2.[60]

Electrochemical performance of the asymmetric supercapacitor

In order to further evaluate the potential of the GNF@$NiCo_2O_4$/MnO_2 electrode in practical applications, ASC was fabricated with GNF@$NiCo_2O_4$/MnO_2 composite and GNF@AC composite

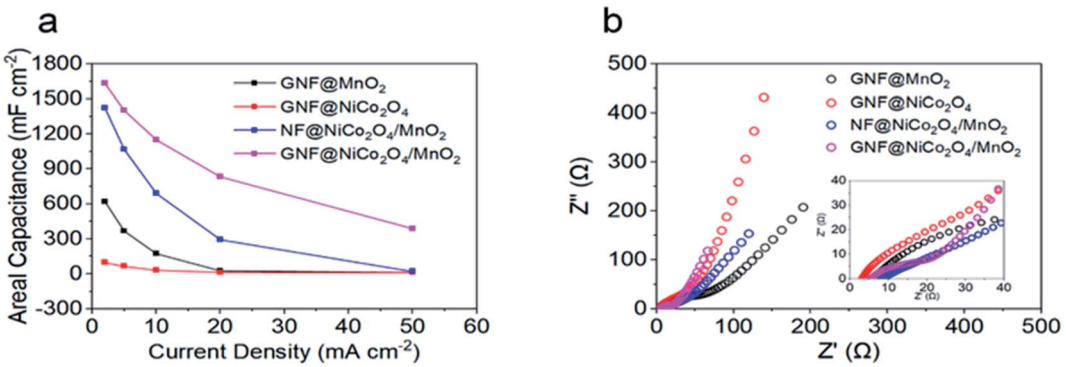

Fig. 7 (a) Areal capacitances of different electrodes at different current densities, (b) Nyquist plots of different samples over a frequency range of 0.01 Hz to 100 kHz.

as the positive and negative, respectively. The electrochemical test of the assembled supercapacitor shows that its large voltage window is 2.1 V, which is beneficial for the promotion of energy density. Fig. 8a shows the CV curve with a voltage window of 1.8 V–2.4 V. Fig. 8b exhibits the CV curves of supercapacitors at different scan rates. The CV curves maintain a good symmetry and are almost rectangular, showing its typical capacitive performance and stable electrochemical performance. The GCD curves of the device at various current densities are depicted in Fig. 8c. Its triangular-like shapes manifest a reversible capacitive behavior. The areal capacitance based on GCD test is calculated to be 824.8 mF cm^{-2} at 2 mA cm^{-2} (Fig. 8d). The reason for the excellent capacitance of the device is mainly due to the heterostructure of the GNF@$NiCo_2O_4$/MnO_2 composite material. The MnO_2 is a petal-like nanosheet with a small thickness. This microstructure ensures high electrochemical utilization of active materials and provides a large surface area and more channels for the enhancement of the electrolyte permeation. $NiCo_2O_4$ is used as a conductive scaffold and its large surface area and rich pore structure provide more growth space for MnO_2, increasing the number of active sites for pseudo-active MnO_2 species, and providing more electron transmission path, thereby realizing a high utilization rate of MnO_2.[61,62] At a high current density of 20 mA cm^{-2}, the fabricated ASC achieves an excellent capacitance retention rate of 80.7% even after 5000 cycles (Fig. 8e). In addition, the capacitance of the supercapacitor shows an increasing trend in the first 500 cycles due to an activation process of the electrode.[63]

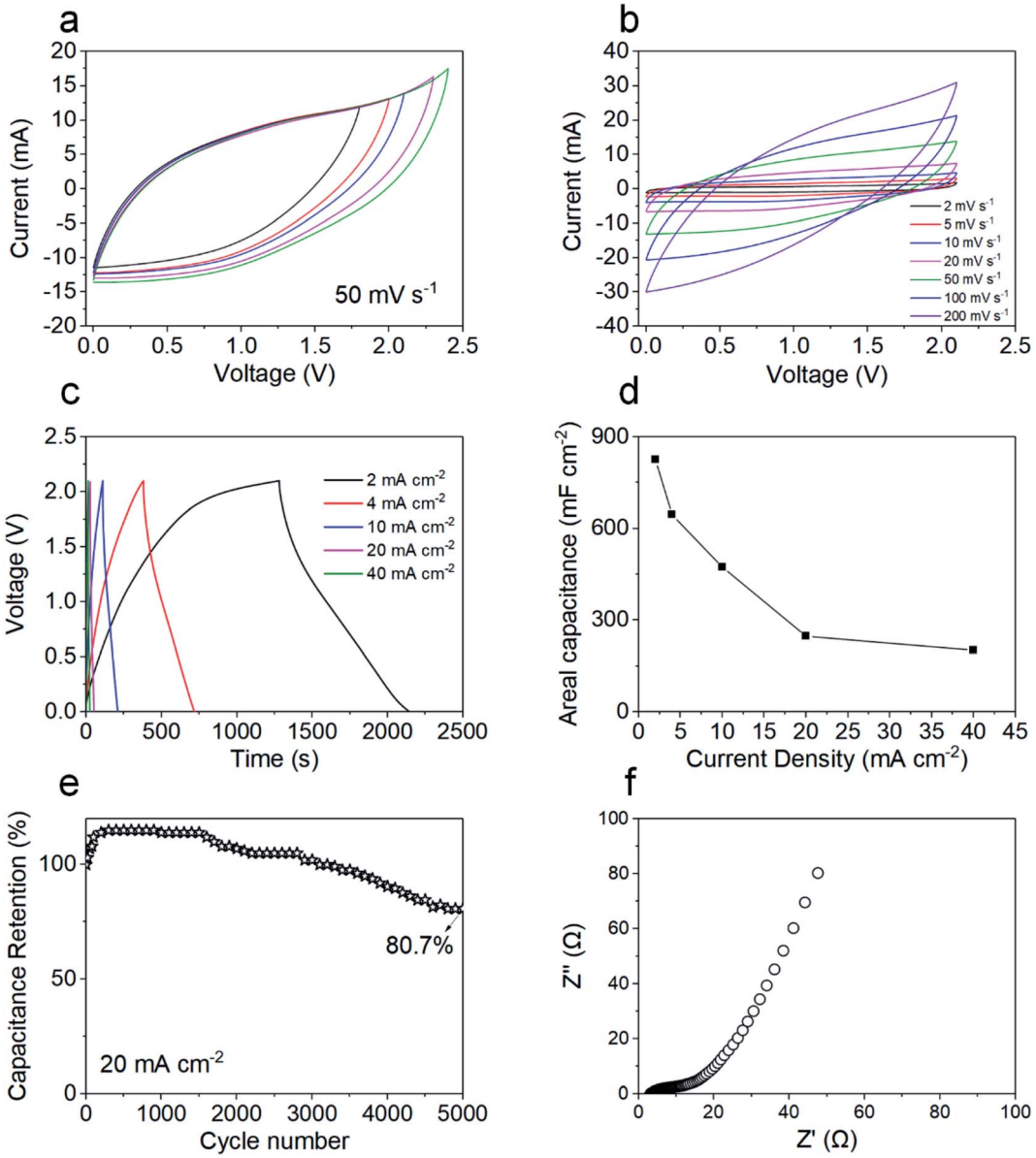

Fig. 8 (a) The CV curves of ASC with different voltage windows, (b) the CV curves of ASC at different scan rates, (c) the GCD curves of ASC at different current densities, (d) GCD profiles of the composite electrodes at different current densities, (e) cyclic stability of the ASC for 2000 cycles at 20 mA cm^{-2}, (f) Nyquist plots of the ASC over a frequency range of 0.01 Hz to 100 kHz.

EIS was performed to test the electrochemical properties of ASC, and the Nyquist plots of the ASC are summarized in Fig. 8f. The Nyquist plots show the impedance R_s of the device is 3.2 Ω and the charge transfer resistance R_{ct} of the device is 13.6 Ω. The high slope in the low frequency region suggests that the supercapacitor possesses low diffusion resistance and excellent capacitive behavior.[64] When its power density is 2100.0 μW cm^{-2} (190.9 W kg^{-1}, 21.0 mW cm^{-3}), the ASC delivers a good specific energy density of 2100.0 μW cm^{-2} (190.9 W kg^{-1}, 21.0 mW cm^{-3}). It possesses better performance than numerous energy storage devices previously reported (Table 1), such as MnO_2/graphene//graphene (30.4 Wh kg^{-1} at 100 W kg^{-1}),[65] NF/$NiCo_2O_4$/MnO_2//AC (35 Wh kg^{-1} at 163 W kg^{-1}),[66] MnO_2/C//N-doped carbon (39.5 Wh kg^{-1} at 200 W kg^{-1}),[28] *et al.*

Accelerated aging tests were also performed under floating conditions after 5000 charge–discharge cycles. The leakage current was recorded during each 2 hours period of constant voltages (1 V–2.1 V) and then the device was permitted to self-discharge for 2 h. As shown in the Fig. S2,† during the leakage current measurements, once the device is fully charged, the leakage current decreases rapidly within seconds and quickly reaches equilibrium. At higher voltages (2 V and 2.1 V), it takes a little longer to reach a plateau. In all cases, however, the leakage current drops sharply to values as low as 250 μA cm^{-2} within a period of 5 minutes. This illustrates the good stability of the cell electrodes. It can be found from Table S1† that the values of leakage currents at different voltages are very small, only 0.007 μA cm^{-2} at 1 V. And as the voltage decreases, the value of leakage current also becomes smaller, which shows that the rate of leakage current depends on the voltage.[67,68] Self-discharge is a spontaneous voltage drop of the energy storage device for a certain storage time, which is detrimental to the voltage and energy retention of the supercapacitor. The self-discharge characteristics can be straightforwardly captured by the time-related voltage retention. Fig. S3† shows the decay of the voltage within 2 h at different starting voltages, and it can be found that the voltage of the supercapacitor decreases gradually with time. It quickly stabilizes at low voltages, and as the voltage increases, it takes longer to reach a stable value. However, at high voltages (1.8 V–2.1 V), the voltage value over 2 h is higher than 1.5 V, which is a generally suitable voltage for supplying power to electronic devices.[72] This proves the potential of the supercapacitor for practical applications. Floating test is a dependable technique for stability analysis of supercapacitor electrode. After the leakage current and self-discharge tests, a float test was performed for 100 hours to further evaluate the stability of the ASC. The voltage was kept at 2.1 V and five GCD cycles were performed at 4 mA cm^{-2} at 10 h intervals. As shown in Fig. 9, the capacity retention value after 100 h of voltage hold is 82.4%, which indicates that the ASC voltage is stable over this voltage window and time. The outstanding performance of the ASC indicates its potential in practical application.

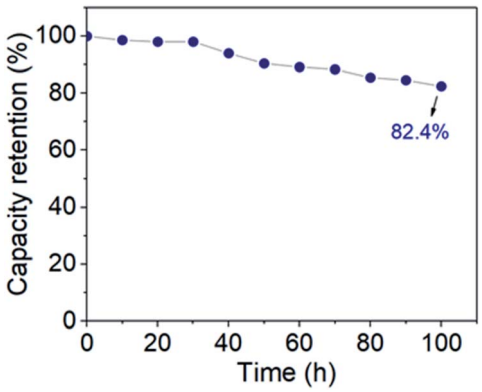

Fig. 9 Floating test of ASC at a constant voltage of 2.1 V for 100 h.

Conclusions

In summary, heterogeneous structured $NiCo_2O_4$/MnO_2 was designed on GNF *via* a convenient two-step hydrothermal method. The petal structured $NiCo_2O_4$ provided large surface area for the growth of high mass loading MnO_2 micro-flowers, which effectively avoided the excessive stacking of high mass-ing loading MnO_2 and increased the electron transmission channel with MnO_2. The addition of graphene buffer layer also effectively improved the rate performance of the electrode

Table 1 Performance comparison between our ASC and other similar supercapacitors

Positive electrode	Electrolyte	Voltage window	Energy density	Power density	Ref.
GNF/$NiCo_2O_4$/MnO_2	KOH	1.6 V	27.8 Wh kg^{-1}	400.3 W kg^{-1}	69
MnO_2/G	Na_2SO_4	2.0 V	30.4 Wh kg^{-1}	100 W kg^{-1}	65
NF/$NiCo_2O_4$/MnO_2	NaOH	1.5 V	35 Wh kg^{-1}	163 W kg^{-1}	66
MnO_2/C	Na_2SO_4	2.0 V	39.5 Wh kg^{-1}	200 W kg^{-1}	28
G/MnO_2	Na_2SO_4	1.8 V	51.1 Wh kg^{-1}	102.2 W kg^{-1}	43
δ-MnO_2	Na_2SO_4	2.0 V	52.22 Wh kg^{-1}	100 W kg^{-1}	61
$NiCo_2O_4$/MnO_2/G	KOH	1.5 V	55.1 Wh kg^{-1}	187.5 W kg^{-1}	15
Na–MnO_2/CNTF//MoS_2/CNTF	Na_2SO_4	2.2 V	178.4 μWh cm^{-2}	1100.9 μW cm^{-2}	70
MnO_2/$NiCo_2O_4$	KOH	1.5 V	0.715 mWh cm^{-3}	353.7 mW cm^{-3}	71
$NiCo_2O_4$/MnO_2	KOH	1.6 V	2.55 mWh cm^{-3}	22 mW cm^{-3}	17
CNT/MnO_2/G/CC	Na_2SO_4	2.2 V	10.18 mWh cm^{-3}	20 mW cm^{-3}	18
GNF/$NiCo_2O_4$/MnO_2	Na_2SO_4	2.1 V	45.9 Wh kg^{-1}, 505.2 μWh cm^{-2}, 5.1 mWh cm^{-3}	190.9 W kg^{-1}, 2100.0 μW cm^{-2}, 21.0 mW cm^{-3}	This work

materials, presenting a high areal capacitance of 1630.5 mF cm^{-2} at 2 mA cm^{-2}. The asymmetric supercapacitor was fabricated by using GNF@$NiCo_2O_4$/MnO_2 as the positive electrode, GNF@AC as the negative electrode, and an environmentally friendly Na_2SO_4 solution as the electrolyte. The ASC reached a wide voltage window of 2.1 V and a high specific energy density of 505.2 μWh cm^{-2} (45.9 Wh kg^{-1}, 5.1 mWh cm^{-3}) at a specific power of 2100.0 μW cm^{-2} (190.9 W kg^{-1}, 21.0 mW cm^{-3}). The superior performance of the asymmetric supercapacitor indicates its practical application for the design of high mass loading supercapacitors.

Conflicts of interest

There are no conflicts to declare.

Acknowledgements

This work was supported by the National Natural Science Foundation of China (Grant no. 51775510, 51875525, 11672269, 11972323, 51572242 and 51675485), the Zhejiang Outstanding Youth Fund (No. LR19E020004), the Zhejiang Provincial Natural Science Foundation of China (Grant no. LR20A020002 and LR18E050002), the Fundamental Research Funds for the Provincial Universities of Zhejiang (RF-B2019004), the 111 Project (No.: D16004).

References

1 N. Choudhary, C. Li, J. Moore, N. Nagaiah, L. Zhai, Y. Jung and J. Thomas, *Adv. Mater.*, 2017, **29**, 1605336.
2 Y. Qiu, Y. Tian, S. Sun, J. Hu, Y. Wang, Z. Zhang, A. Liu, H. Cheng, W. Gao, W. Zhang, H. Chai and H. Wu, *Nano Energy*, 2020, **78**, 105337.
3 Y. Yu, X. Xu, C. Lu, T. Zhang and Y. Ma, *Thin Solid Films*, 2020, **712**, 138302.
4 X. Xiong, G. Waller, D. Ding, D. Chen, B. Rainwater, B. Zhao, Z. Wang and M. Liu, *Nano Energy*, 2015, **16**, 71–80.
5 Z. Yang and X. Liang, *Nano Res.*, 2020, **13**, 461–466.
6 Y. Liu, M. Hu, M. Zhang, L. Peng, H. Wei and Y. Gao, *J. Alloys Compd.*, 2017, **696**, 1159–1167.
7 S. Cho, J. Kim, Y. Jo, A. T. A. Ahmed, H. S. Chavan, H. Woo, A. I. Inamdar, J. L. Gunjakar, S. M. Pawar, Y. Park, H. Kim and H. Im, *J. Alloys Compd.*, 2017, **725**, 108–114.
8 S. Kong, K. Cheng, T. Ouyang, Y. Gao, K. Ye, G. Wang and D. Cao, *Electrochim. Acta*, 2017, **246**, 433–442.
9 H. Jiang, X. Cai, Y. Qian, C. Zhang, L. Zhou, W. Liu, B. Li, L. Lai and W. Huang, *J. Mater. Chem. A*, 2017, **5**, 23727–23736.
10 J. Zhou, Y. Huang, X. Cao, B. Ouyang, W. Sun, C. Tan, Y. Zhang, Q. Ma, S. Liang, Q. Yan and H. Zhang, *Nanoscale*, 2015, **7**, 7035–7039.
11 H. Jiang, J. Ma and C. Li, *Chem. Commun.*, 2012, **48**, 4465–4467.
12 T. Zhai, F. Wang, M. Yu, S. Xie, C. Liang, C. Li, F. Xiao, R. Tang, Q. Wu, X. Lu and Y. Tong, *Nanoscale*, 2013, **5**, 6790–6796.
13 H. Jiang, C. Li, T. Sun and J. Ma, *Nanoscale*, 2012, **4**, 807–812.
14 J. A. Yan, E. Khoo, A. Sumboja and P. S. Lee, *ACS Nano*, 2010, **4**, 4247–4255.
15 M. A. Garakani, S. Abouali, Z.-L. Xu, J. Huang, J.-Q. Huang and J.-K. Kim, *J. Mater. Chem. A*, 2017, **5**, 3547–3557.
16 X. Lu, T. Zhai, X. Zhang, Y. Shen, L. Yuan, B. Hu, L. Gong, J. Chen, Y. Gao, J. Zhou, Y. Tong and Z. L. Wang, *Adv. Mater.*, 2012, **24**, 938–944.
17 J. Zhang, Y. Wang, C. Yu, T. Zhu, Y. Li, J. Cui, J. Wu, X. Shu, Y. Qin, J. Sun, J. Yan, Y. Zhang and Y. Wu, *J. Mater. Sci.*, 2019, **55**, 688–700.
18 L. Lyu, K.-d. Seong, J. M. Kim, W. Zhang, X. Jin, D. K. Kim, Y. Jeon, J. Kang and Y. Piao, *Nano-Micro Lett.*, 2019, **11**, 88.
19 M.-S. Balogun, H. Yang, Y. Luo, W. Qiu, Y. Huang, Z.-Q. Liu and Y. Tong, *Energy Environ. Sci.*, 2018, **11**, 1859–1869.
20 Z. Pan, M. Liu, J. Yang, Y. Qiu, W. Li, Y. Xu, X. Zhang and Y. Zhang, *Adv. Funct. Mater.*, 2017, **27**, 1701122.
21 B. Yao, S. Chandrasekaran, J. Zhang, W. Xiao, F. Qian, C. Zhu, E. B. Duoss, C. M. Spadaccini, M. A. Worsley and Y. Li, *Joule*, 2019, **3**, 459–470.
22 N. R. Chodankar, S. J. Patil, G. S. Rama Raju, D. W. Lee, D. P. Dubal, Y. S. Huh and Y. K. Han, *ChemSusChem*, 2020, **13**, 1582–1592.
23 C. Lu, F. Shi, J. Jin and X. Peng, *Materials*, 2019, **12**, 899.
24 M. L. Li, D. H. Liu, D. C. Wei, X. F. Song, D. P. Wei and A. T. S. Wee, *Adv. Sci.*, 2016, **3**, 1600003.
25 Y. Ma, M. Wang, N. Kim, J. Suhr and H. Chae, *J. Mater. Chem. A*, 2015, **3**, 21875–21881.
26 Z. Bo, S. Mao, Z. J. Han, K. F. Cen, J. H. Chen and K. Ostrikov, *Chem. Soc. Rev.*, 2015, **44**, 2108–2121.
27 M. Cai, R. A. Outlaw, S. M. Butler and J. R. Miller, *Carbon*, 2012, **50**, 5481–5488.
28 Y. Dai, L. Chen, V. Babayan, Q. Cheng, P. Saha, H. Jiang and C. Li, *J. Mater. Chem. A*, 2015, **3**, 21337–21342.
29 V. Khomenko, E. Raymundo-Piñero and F. Béguin, *J. Power Sources*, 2006, **153**, 183–190.
30 H. Gao, F. Xiao, C. B. Ching and H. Duan, *ACS Appl. Mater. Interfaces*, 2012, **4**, 7020–7026.
31 M. D. Stoller and R. S. Ruoff, *Energy Environ. Sci.*, 2010, **3**, 1294–1301.
32 K. Tao, Y. Yang, C. Yang, Q. Ma and L. Han, *Dalton Trans.*, 2019, **48**, 14156–14163.
33 H. Gao, F. Xiao, C. B. Ching and H. Duan, *ACS Appl. Mater. Interfaces*, 2012, **4**, 2801–2810.
34 T. Brousse, M. Toupin and D. Bélanger, *J. Electrochem. Soc.*, 2004, **151**, A614–A622.
35 X. Jia, X. Wu and B. Liu, *Dalton Trans.*, 2018, **47**, 15506–15511.
36 G. Ren, X. Pan, S. Bayne and Z. Fan, *Carbon*, 2014, **71**, 94–101.
37 J. Sha, C. Gao, S. K. Lee, Y. Li, N. Zhao and J. M. Tour, *ACS Nano*, 2016, **10**, 1411–1416.
38 A. C. Ferrari, J. C. Meyer, V. Scardaci, C. Casiraghi, M. Lazzeri, F. Mauri, S. Piscanec, D. Jiang, K. S. Novoselov, S. Roth and A. K. Geim, *Phys. Rev. Lett.*, 2006, **97**, 187401.

39 Z. Z. Sun, A. R. O. Raji, Y. Zhu, C. S. Xiang, Z. Yan, C. Kittrel, E. L. G. Samuel and J. M. Tour, *ACS Nano*, 2012, **6**, 9790–9796.
40 Y. Hao, Y. Wang, L. Wang, Z. Ni, Z. Wang, R. Wang, C. K. Koo, Z. Shen and J. T. Thong, *Small*, 2010, **6**, 195–200.
41 C. Zhang, T. Kuila, N. H. Kim, S. H. Lee and J. H. Lee, *Carbon*, 2015, **89**, 328–339.
42 V. H. Nguyen and J.-J. Shim, *J. Power Sources*, 2015, **273**, 110–117.
43 Z. Fan, J. Yan, T. Wei, L. Zhi, G. Ning, T. Li and F. Wei, *Adv. Funct. Mater.*, 2011, **21**, 2366–2375.
44 Q. Y. Shan, X. L. Guo, F. Dong and Y. X. Zhang, *Mater. Lett.*, 2017, **202**, 103–106.
45 Y. Huang, C. Shen, Z. Tang, T. Shi, S. Zheng and L. Lin, *ChemElectroChem*, 2019, **6**, 6009–6015.
46 W. Xu, Y. Xing, J. Liu, H. Wu, Y. Cui, D. Li, D. Guo, C. Li, A. Liu and H. Bai, *ACS Nano*, 2019, **13**, 7930–7938.
47 X. Zheng, J. Luo, W. Lv, D. W. Wang and Q. H. Yang, *Adv. Mater.*, 2015, **27**, 5388–5395.
48 L. Zhuang, L. Ge, Y. Yang, M. Li, Y. Jia, X. Yao and Z. Zhu, *Adv. Mater.*, 2017, **29**, 1606793.
49 H. Chen and J. Wang, *Chemosphere*, 2021, **268**, 128840.
50 J.-C. Dupin, D. Gonbeau, P. Vinatier and A. Levasseur, *Phys. Chem. Chem. Phys.*, 2000, **2**, 1319–1324.
51 S. Bag and C. R. Raj, *J. Mater. Chem. A*, 2016, **4**, 8384–8394.
52 Z. Lei, J. Zhang and X. S. Zhao, *J. Mater. Chem.*, 2012, **22**, 153–160.
53 L. Du, X. Song, X. Liang, Y. Liu and M. Zhang, *Appl. Surf. Sci.*, 2020, **526**, 146706.
54 L. Sha, K. Ye, G. Wang, J. Shao, K. Zhu, K. Cheng, J. Yan, G. Wang and D. Cao, *J. Power Sources*, 2019, **412**, 265–271.
55 P. Salarizadeh, M. B. Askari, M. Seifi, S. M. Rozati and S. S. Eisazadeh, *Mater. Sci. Semicond. Process.*, 2020, **114**, 105078.
56 Z. H. Huang, Y. Song, D. Y. Feng, Z. Sun, X. Sun and X. X. Liu, *ACS Nano*, 2018, **12**, 3557–3567.
57 G. Liu, X. Kong, H. Sun and B. Wang, *Ceram. Int.*, 2014, **40**, 14391–14395.
58 X. Kong, H. Sun, Z. Yi, B. Wang, G. Zhang and G. Liu, *Ceram. Int.*, 2017, **43**, 13394–13400.
59 J. W. Mao, C. H. He, J. Q. Qi, A. B. Zhang, Y. W. Sui, Y. Z. He, Q. K. Meng and F. X. Wei, *J. Electron. Mater.*, 2017, **47**, 512–520.
60 Z. Bo, W. Zhu, W. Ma, Z. Wen, X. Shuai, J. Chen, J. Yan, Z. Wang, K. Cen and X. Feng, *Adv. Mater.*, 2013, **25**, 5799–5806.
61 C. H. Wang, H. C. Hsu and J. H. Hu, *J. Power Sources*, 2014, **249**, 1–8.
62 X. Li, Z. Wang, L. Guo, D. Han, B. Li and Z. Gong, *Electrochim. Acta*, 2018, **265**, 71–77.
63 C. Wu, Y. Zhu, M. Ding, C. Jia and K. Zhang, *Electrochim. Acta*, 2018, **291**, 249–255.
64 L. G. Beka, X. Li and W. Liu, *Sci. Rep.*, 2017, **7**, 2105.
65 Z. S. Wu, W. C. Ren, D. W. Wang, F. Li, B. L. Liu and H. M. Cheng, *ACS Nano*, 2010, **4**, 5835–5842.
66 K. Xu, W. Li, Q. Liu, B. Li, X. Liu, L. An, Z. Chen, R. Zou and J. Hu, *J. Mater. Chem. A*, 2014, **2**, 4795–4802.
67 M. Haque, Q. Li, A. D. Smith, V. Kuzmenko, P. Rudquist, P. Lundgren and P. Enoksson, *J. Power Sources*, 2020, **453**, 227897.
68 B. E. Conway, W. G. Pell and T. C. Liu, *J. Power Sources*, 1997, **65**, 53–59.
69 H. Chen, C.-K. Hsieh, Y. Yang, X. Y. Liu, C.-H. Lin, C.-H. Tsai, Z. Q. Wen, F. Dong and Y. X. Zhang, *ChemElectroChem*, 2017, **4**, 2414–2422.
70 Q. Zong, Q. Zhang, X. Mei, Q. Li, Z. Zhou, D. Li, M. Chen, F. Shi, J. Sun, Y. Yao and Z. Zhang, *ACS Appl. Mater. Interfaces*, 2018, **10**, 37233–37241.
71 S. Khalid, C. Cao, L. Wang, Y. Zhu and Y. Wu, *RSC Adv.*, 2016, **6**, 70292–70302.
72 M. Y. Xia, J. H. Nie, Z. L. Zhang, X. M. Lu and Z. L. Wang, *Nano Energy*, 2018, **47**, 43–50.